Shielding an MCP detector for a space-borne mass spectrometer against the harsh radiation environment in Jupiter's Magnetosphere

D. Lasi[1], M. Tulej[1,a], S. Meyer[1], M. Lüthi[1], A. Galli[1], D. Piazza[1], P. Wurz[1], D. Reggiani[2], H. Xiao[2], R. Marcinkowski[2], W. Hajdas[2], A. Cervelli[3], S. Karlsson[4], T. Knight[5], M. Grande[5], and S. Barabash[4].

***Abstract*—Detectors of scientific instruments on spacecraft flying through Jupiter radiation belts need to be protected from high fluxes of penetrating radiation by means of radiation shields. Electrons constitute the most difficult component of Jupiter's magnetosphere to shield from, because of their abundance, penetration depth in matter, and intensity of bremsstrahlung radiation generated upon interaction with the shielding material. For the Neutral and Ion Mass spectrometer (NIM) of the Particle Environment Package (PEP) instrument suite on board the European Space Agency's mission JUpiter Icy moons Explorer (JUICE), we devised a shielding design made of an aluminum and tantalum stack to reduce the radiation-induced noise on its Micro-Channel Plate (MCP) detector. To predict the expected radiation background in the mass spectra in space, we manufactured a flight-like shielded detector and submitted it to radiation testing at the Paul Scherrer Institut with an electron beam in the energy range ~30 to ~345 MeV. The results of this test provide a verification of the NIM capability to fulfill its science requirements in the mission's worst-case scenario (the Europa flyby), and give insights into new directions of optimization of shielding elements' design for NIM and similar instrument bound to operate in a harsh radiation environment.**

***Index Terms*—Jupiter, Micro-Channel Plate, Mass spectrometry, Radiation detectors, Space exploration, electron beams, Radiation shielding.**

I. Introduction

The Neutral and Ion Mass spectrometer (NIM) is a Time-Of-Flight (TOF) mass spectrometer and part of the Particle Environment Package (PEP) on board of Jupiter Icy moons Explorer (JUICE) mission of the European Space Agency (ESA). It will investigate the exospheres of Jupiter's icy moons Europa, Ganymede, and Callisto by providing the first in-situ characterization of their chemical composition in terms of neutral and ionized atoms and molecules. The achievement of these science goals depends critically on the efficacy of its detector's radiation shielding to attenuate the measurement background induced by the instantaneous fluxes of penetrating radiation that is abundant within Jupiter's radiation belts. Indeed, the MCP is both sensitive to the measured ions proper – the time-correlated signal of the TOF system – and to penetrating radiation including electrons (e^-), positrons (e^+), protons (p^+) and gammas (γ), which generates a time-uncorrelated noise in the spectra.

The worst and sizing case for NIM radiation shielding is the flyby of Europa: the innermost satellite explored by JUICE where the highest fluxes of penetrating radiation are encountered [1], and where NIM will provide an unprecedented opportunity to shed light on the composition of this potentially habitable world. The radiation environment at Europa is characterized by high-fluxes of e^- and p^+, of the order of 10^7 and 10^6 # cm^{-2} sr^{-1} s^{-1} MeV^{-1}, respectively. Electrons are the most difficult energetic particles to shield. First, because their range in shielding materials is about two decades higher than for p^+ (e.g., for Al, 10s MeV e^- cross several mm-thick shields, whereas p^+ are stopped after few μm). Second, because e^- produce intense bremsstrahlung radiation upon interaction with the shielding. Third, because the energy spectrum of e^- at Jupiter extends to energies up to hundreds MeV with fluxes as high as 10^1 to 10^2 # cm^{-2} sr^{-1} s^{-1} MeV^{-1}, whereas the p^+ flux is about two decades lower. All in all, instantaneous e^- fluxes in the energy range of 10s to 100s MeV represent the most critical fraction of the radiation spectrum at Jupiter for any instrument affected by instantaneous fluxes of penetrating particles on their detectors.

The goal of this investigation is to verify experimentally that the flight design of the NIM detector radiation shields (Fig. 1) provides a sufficient background radiation attenuation in the Jupiter environment. We build upon previous investigations on the detection efficiency of MCPs to

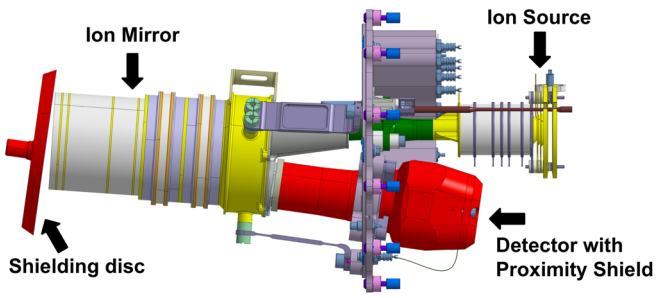

Fig. 1: The NIM instrument mass analyzer design showing the main elements of the ion optics and, in red, the two shielding elements. The mass of the proximity shield and of the shielding disc are 1027 g and 465 g, respectively.

This work was supported by the ESA PRODEX programme.
a) Corresponding author: marek.tulej@space.unibe.ch
1) Space Research and Planetary Science, Physics Institute, University of Bern (CH 3012 Bern, Switzerland).
2) Paul Scherrer Institut, PSI (CH 5232 Villigen, Switzerland).
3) Laboratory for High Energy Physics, Physics Institute, University of Bern (CH 3012 Bern, Switzerland).
4) Swedish Institute of Space Physics/IRF (981 28 Kiruna, Sweden).
5) University of Aberystwyth (SY23 3FL Aberystwyth, United Kingdom).

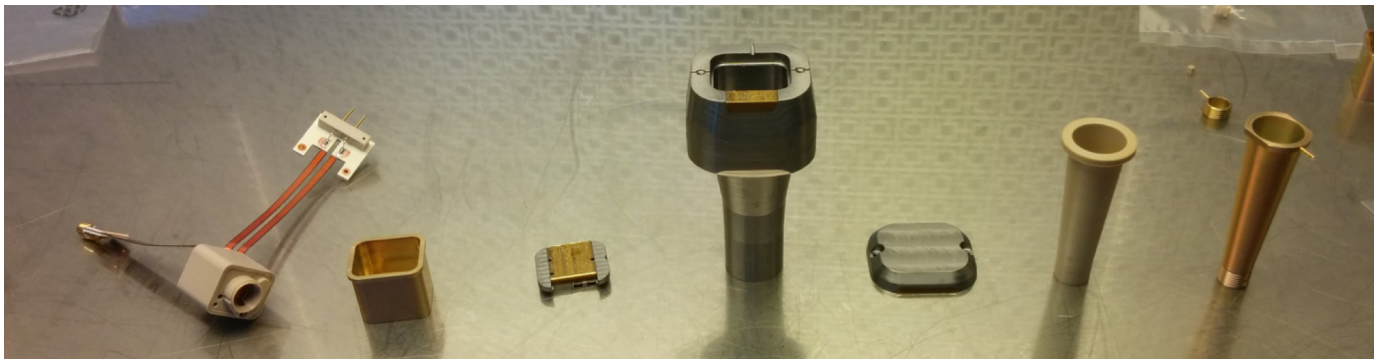

Fig. 2: From left to right: MCP detector assembly inside its PEEK housing, 1 mm thick Al detector housing, 1mm and Al and Ta detector back-cover, main Ta proximity shielding element, Ta proximity shielding back-cover, PEEK insulator between the Ta shielding (grounded) and 1 mm Al-thick drift tube (at –2.5 kV).

energetic electrons [2] and on their shielding efficiency by means of Al and Ta shields [3], and performed a new experiment at the Paul Scherrer Institut (PSI) on a flight-representative detector with e^- in the range of momenta 20 to 345 MeV/c (which correspond to a kinetic energy of ~20 to ~345 MeV, because of the small e^- rest mass of 0.511 MeV). Based on the experimental count rates and on the expected radiation environment in space [1], we predict the background noise level in the mass spectra at Europa, and discuss how this relates to the NIM instruments science goals. Given that NIM is the first TOF mass spectrometer to be employed in Jupiter's radiation belts, this study provides the first concept of a mass-efficient radiation shielding for any instrument of its kind bound to operate in a harsh radiation environment.

II. DETECTOR DESIGN

The NIM detector assembly (Fig. 2) is made of two identical Micro-Channel Plates (MCPs) from Photonis USA Inc., of 10 mm diameter, with an active area diameter of 8 mm, mounted in chevron configuration. The channels have a pore diameter of 10 μm and a center-to-center spacing of 12 μm, for an Open Area Ratio (OAR) of 67%. The channels' angle is 8°. The ΔV across the two plates can be between –1.8 and –2.2 kV, for an amplification stage of ~10^3 per plate and a total gain of 10^6 to 10^7 in the middle of this range [2]. According to ion optics requirements, a gold-plated grid at drift potential is placed in front of the MCP stack, and the electrical potential of the whole detector is kept floating with respect to ground. Anode and signal chain are impedance-matched to 50 Ω.

The proximity electronics of the detector is spread over a combination of rigid and flex printed circuit boards, to allow for folding the detector with its electronics in a cuboid volume of 22 × 18 × 16 mm (Fig. 2). This design is optimized for high-speed (1 ns pulses) and small-volume. The former is driven by performance requirement (e.g., mass resolution, M/ΔM>1100), whereas the latter is driven by the need of minimizing shielding mass: a scarce resource on a spacecraft.

In space, the detector is operated in analog mode and the signal generated by the incoming particles (ions or penetrating radiation) is acquired by a 10-bit analog-to-digital converter (ADC), which digitizes it at the rate of 2.0 Gigasamples/s. The TOF operates at 10 kHz repetition rate, and waveforms are summed in the field-programmable gate array (FPGA) for typically 5 s at flyby closest approach to provide TOF-histograms – the actual data product downlinked to Earth after compression – which are converted on-ground to calibrated mass spectra.

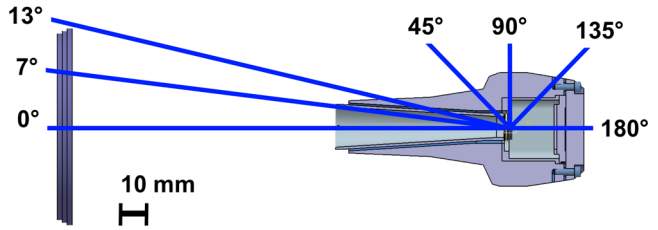

Fig. 3: Section of the NIM detector showing the shielding elements and the investigated angles of incidence of the beam on the MCP.

III. SHIELDING DESIGN

Previous modelling of the radiation background shielding considered MCP plates hypothetically fully enclosed in a cylindrical shield [6]. These studies showed that an Al–Ta–Al sandwich provides for the most mass-efficient solution to suppress the e^--induced radiation background. This is found to be in a good agreement with the general shielding design principle inherited by dose-related studies [5]. In combination with the results of subsequent simulations [7], which accounted for both the evolution of the mission profile and of the NIM instrument design, the current shielding baseline comprises (Fig. 1):

- A *proximity shield* around the detector, made of 1 mm Al – 10 mm Ta – 1 mm Al layered stack in each direction in the line of sight of MCP, with a cone of shielding material protruding towards the direction of the ions.
- A *shielding disc* of 80 mm diameter placed behind the NIM instrument ion mirror (i.e., 176 mm away from the MCP), made of a 1 mm Al – 6 mm Ta sandwich.

The actual shape of both elements (Fig. 2) has been optimized [7] for minimal mass through Geant4 simulations of ~500 geometries covering a solution space bounded by the requirements of completely closing the Field-of-View (FoV) of the MCPs while not protruding with shielding elements into the mass spectrometer's ion trajectories.

IV. EXPERIMENTAL METHOD

A. Vacuum Chamber

The ion detector is kept in a lightweight vacuum chamber that was designed and manufactured specifically for this experiment (Fig. 5). The chamber consists of a hemispherical shell of 1 mm Al thickness, bolted on a stainless steel plate upon which the shielded detector is mounted such that the MCP is in the center of the sphere at a height of about 95 mm above the baseplate. All the detector supporting elements are made of PEEK (polyetheretherketone) or fiberglass to minimize their role in generating secondaries upon interaction with the beam. The baseplate support allows to mount shielding discs of different thicknesses outside the chamber, at a distance representative of the flight instrument's geometry.

The primary beam is focused on the vacuum chamber wall and the entire chamber is rotated with a motorized mechanism to accurately change the angle of incidence of the incoming particle beam on the detector. The angle is defined with respect to the normal to the MCP surface. The shielded detector is approximately of cylindrical symmetry; therefore, a single angle scan from 0 to 180° in the plane of the baseplate is sufficient to calculate detector response to a three-dimensional environment.

B. Detector and Shielding

A flight-representative MCP detector, including radiation shielding, has been built for this test (Fig. 4). The only deviation from the flight design is the lack of the external 1 mm Al layer of the Al–Ta–Al sandwich, which is not implemented as the vacuum chamber already provides for a 1 mm Al hemispherical layer outside the detector.

Different configurations of the shielding disc are tested with 4, 6, and 8 Ta thicknesses at 0° angle. Moreover, we perform a measurement also without the shielding disc and for a completely unshielded detector. In this case, the innermost 1 mm Al layer that is foreseen on the plate is not implemented, because the vacuum chamber already provides it. The full angle scan of the detector is performed with the 6 mm Ta shielding disc (baseline disc thickness) mounted outside the chamber.

The MCP detector is operated at –2.0 kV, corresponding to an effective voltage per plate of –913 V. The detector is kept floating on a high voltage such that the entrance of the detector (the grid) is at –2.5 kV, the drift voltage of the NIM instrument. Compared to our previous studies [2] and [3], for this investigation we use a higher voltage within the foreseen range of operation in space (–2.0 to –2.2 kV), which leads to a gain approximately four times higher.

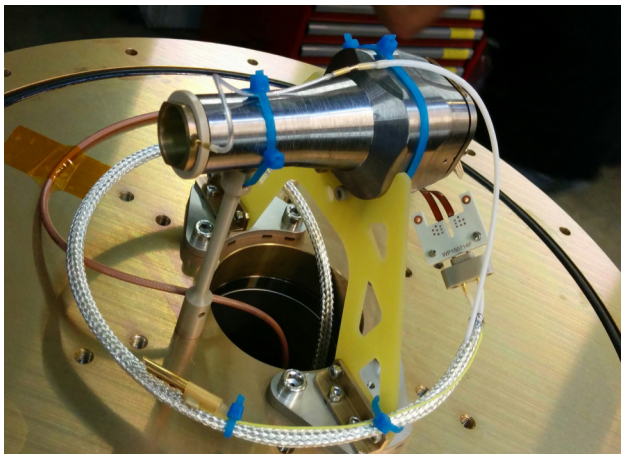

Fig. 4: Shielded detector mounted on the vacuum chamber baseplate.

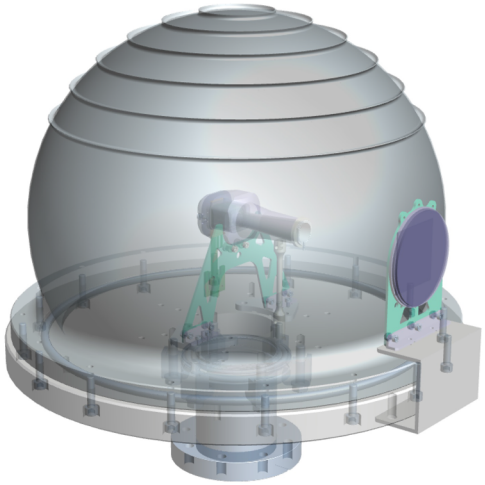

Fig. 5: Vacuum chamber model comprising, in the center, the shielded MCP detector. The hemispherical shell is made of 1 mm Al (∅ ~350 mm). To the right, the shielding discs mounted on an external support are visible. The bottom tube is connected to an oil-free rotary vacuum pump.

C. Beam and experiment area

Experiments are performed on the secondary pion beamline (PiM1) of the High-Intensity Proton Accelerator facility at PSI. A pure e^- beam is delivered for beam momenta ≤ 86.25 MeV/c [4]. At higher momenta, the particle beam contains also some fractions of muons (μ^-) and pions (π^-) (Table I). Nevertheless, the contribution of these particles to the signal generated by MCP detector can be well isolated using the time-of-flight method described in previous publications [2] and [3].

The vacuum chamber is placed in front of the last focussing magnet of the beam line, with its wall at the beam focal plane. The MCP measurements of the secondary particles generated in the radiation shielding material are acquired by an oscilloscope placed in the beam area, and operated remotely from the control room [2, 3]. A controlling software not only stores all acquired waveforms at the end of the acquisition, but also records several parameters in real time, including the beam 50 MHz trigger signal and the beam current, so that any

TABLE I
BEAM FRACTIONS

Beam p (MeV/c)	e^- (%)	η^- (%)	π^- (%)	e^- E_K (MeV)
20	100	0.0	0.0	19.50
30	100	0.0	0.0	29.49
50	100	0.0	0.0	49.49
86.25	100	0.0	0.0	85.74
115	97.5	0.7	1.9	114.49
143.75	83.8	2.1	14.2	143.24
172.50	63.2	2.4	34.5	171.99
201.25	46.4	2.2	51.4	200.74
230	30.4	0.0	69.6	229.49
287.50	14.0	0.0	86.0	286.99
345	6.9	0.0	93.1	344.49

This article has been accepted for publication in a future issue of this journal, but has not been fully edited. Content may change prior to final publication. Citation information: DOI 10.1109/TNS.2016.2614040, IEEE Transactions on Nuclear Science

instability of the beam is detected in real time. In those (rare) cases the measurement is immediately repeated. The vacuum chamber rotation is commanded from remote, and the angle is verified by means of a webcam pointed at a goniometer.

This paper presents in detail only the data relative to the e^- fraction of the particle beam. Because the space environmental specifications are given in terms of energy and not momentum, the electrons' kinetic energy (E_K) calculated via Eq. 1 is also given in Table I.

$$E_K = \sqrt{p^2 + m_0c^2} - m_0c^2 \quad (1)$$

D. Data acquisition and analysis

An oscilloscope stores all the waveforms of duration of 20 ns with the signals exceeding a certain trigger level, which is set to –2.5 mV (for background radiation measurements) or –4.0 / –7.0 mV (for measurements with the particle beam). The acquisition of a minimum number of waveforms (3,000–10,000, depending on the beam momentum) is targeted, and both the total acquisition time and each waveform's time-stamp are recorded for the subsequent calculation of the count rates. This set of waveforms is processed afterwards with MATLAB, to separate the populations of pulses belonging to e^-, μ^-, and π^- based on their time difference with the 50 MHz beam trigger [2,3]. After subtraction of background, the Pulse Height Distribution (PHD) and the charge per pulse distribution are plotted for the electrons' population of the complete set of waveforms.

For all measurements, both the PHD and the charge pulse height distribution show a characteristic negative exponential shape [2, 3]. The total detector count rate is derived by extrapolation of the charge per pulse distribution to zero and subsequent integration.

V. Results And Discussion

A. Beam Diagnostic Measurements

The PiM1 facility provides a stable particle beam production with a frequency of 50 MHz and an average proton current of 2.2 mA. The beam profile is characterized with a beam scanner, which measures the total beam current in *x*- and *y*-direction, for the following configurations:

a) position of the vacuum chamber wall (i.e., beam focus)
b) center of the vacuum chamber (i.e., MCP location)
c) center of the vacuum chamber, with a large 1 mm Al plate placed at the beam focus, so that the measurement reflects the beam conditions inside the vacuum chamber.

The measured beam profile is fitted with a 2D-gaussian to derive the beam maximum flux and intensity (Table II).

For momenta higher than 30 MeV/c, the beam intensity is large enough to allow for a good statistics and a good fitting of the beam scanner profiles. Besides, the maximum beam flux and intensity are affected only by 0.1% to 3.6% and by 0.2% to 4%, respectively, by the presence of the 1 mm Al plate (compare configurations b) and c) in Table II). Therefore, we can consider the vacuum chamber to be transparent to e^- for beam momenta larger than 30 MeV/c for the practical effects of this investigation.

The measurements at 20 and 30 MeV/c are affected by two issues. First, the beam intensity is very low, and the low statistics of the scanner measurements leads to an error on flux and intensity that we estimate to be close to ~25%. Second, between configurations b) and c) presence of 1 mm Al leads to

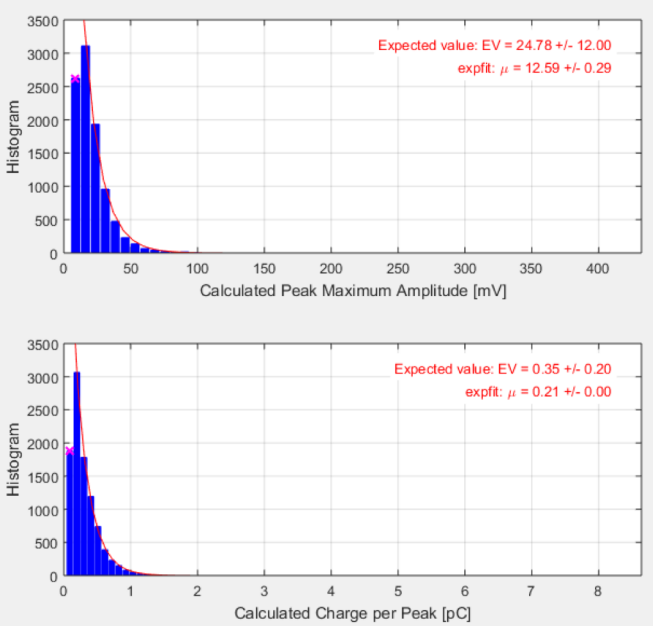

Fig. 6: Example of pulse height (top) and charge per pulse (bottom) distribution for the same set of waveforms. The exponential fitting curve and parameters are shown in red. 115 MeV/c, 0°, on nominally shielded detector.

TABLE II
Beam Characteristics

p (MeV/c)	Configuration	Max. Flux (# s^{-1} cm^{-2} mA^{-1})	Intensity (# s^{-1} mA^{-1})	σ_x (mm)	σ_y (mm)
20	a)	3.8×10^2	1.55×10^4	23.4	27.6
	b)	2.68×10^2	5.21×10^4	57.3	53.9
	c)	6.9×10^1	4.57×10^3	30.4	34.7
30	a)	1.32×10^3	6.26×10^4	24.6	30.8
	b)	1.04×10^3	8.48×10^4	31.9	40.5
	c)	9.75×10^2	5.35×10^4	26.6	32.9
50	a)	6.77×10^4	2.28×10^6	20.4	26.3
	b)	4.98×10^4	2.30×10^6	25.1	29.3
	c)	4.80×10^4	2.31×10^6	25.7	29.9
86.25	a)	2.73×10^5	6.65×10^6	17.1	22.7
	b)	2.10×10^5	6.67×10^6	20.6	24.5
	c)	2.11×10^5	6.94×10^6	21.1	24.8
115	a)	3.47×10^5	7.44×10^6	18.4	18.6
	b)	3.45×10^5	7.16×10^6	15.5	21.4
	c)	3.46×10^5	7.22×10^6	15.7	21.2
143.75	a)	4.87×10^5	9.16×10^6	17.8	16.9
	b)	4.98×10^5	9.05×10^6	14.9	19.4
	c)	4.98×10^5	9.18×10^6	15.2	19.4
172.50	a)	6.91×10^5	1.19×10^7	17.1	16.1
	b)	7.11×10^5	1.18×10^7	14.3	18.5
	c)	7.03×10^5	1.18×10^7	14.5	18.5
201.25	a)	1.01×10^6	1.56×10^7	16.5	14.8
	b)	1.02×10^6	1.54×10^7	13.9	17.3
	c)	1.01×10^6	1.54×10^7	14.0	17.3
230	a)	1.43×10^6	1.99×10^7	16.1	13.8
	b)	1.45×10^6	2.00×10^7	13.6	16.2
	c)	1.44×10^6	1.98×10^7	13.5	16.2
287.50	a)	2.32×10^6	2.74×10^7	15.7	12.0
	b)	2.41×10^6	2.79×10^7	13.0	14.2
	c)	2.36×10^6	2.75×10^7	13.0	14.3
345	a)	4.41×10^6	3.04×10^7	9.7	11.3
	b)	4.09×10^6	3.13×10^7	10.3	11.8
	c)	3.97×10^6	3.07×10^7	10.4	11.8

For a description of configurations a), b), and c), refer to the text (Section V).

TABLE III
DETECTOR COUNT RATE BEHIND SHIELDING

e^- E_K (MeV)	0°	7°	13°	45°	90°	135°	180°	∫dφ
29.49	3.76×10^1	N/A	N/A	5.54×10^1	N/A	4.68×10^1	4.12×10^1	5.02×10^1*
49.49	1.18×10^3	9.91×10^2	1.45×10^3	3.09×10^3	2.68×10^3	2.58×10^3	2.52×10^3	2.66×10^3
85.74	1.55×10^4	1.07×10^4	1.31×10^4	3.27×10^4	2.70×10^4	2.95×10^4	2.91×10^4	2.75×10^4
114.49	3.07×10^4	2.23×10^4	2.99×10^4	6.75×10^4	5.33×10^4	6.52×10^4	6.72×10^4	5.61×10^4
143.24	5.38×10^4	4.14×10^4	4.82×10^4	1.29×10^5	9.94×10^4	1.18×10^5	1.20×10^5	1.04×10^5
171.99	7.92×10^4	6.76×10^4	7.30×10^4	1.61×10^5	1.35×10^5	1.62×10^5	1.72×10^5	1.40×10^5
200.74	9.56×10^4	8.09×10^4	8.78×10^4	2.10×10^5	1.47×10^5	1.90×10^5	1.91×10^5	1.59×10^5
229.49	9.88×10^4	7.84×10^4	9.50×10^4	1.93×10^5	1.55×10^5	1.99×10^5	1.84×10^5	1.64×10^5
286.99	8.26×10^4	6.95×10^4	7.54×10^4	N/A	1.24×10^5	1.52×10^5	1.57×10^5	1.12×10^5
344.49	6.37×10^4	4.69×10^4	5.12×10^4	1.03×10^5	8.32×10^4	1.01×10^5	1.11×10^5	8.75×10^4

Units for count rates: # cm^{-2} MeV^{-1}. The last column reports the numerical integral over the whole sphere. N/A means that data are not available. * = this integral is calculated using the reduced set of angles that is available at this momentum, by assigning a higher numerical integration weight to the available angles.

a significant reduction of beam intensity (–91% and –37% at 20 and 30 MeV/c), thus making the statistics of the data for configuration c) particularly poor and showing that the vacuum chamber may affect the beam properties. The combination of these factors forces us to discard all data at 20 MeV/c and report only a limited set of results at 30 MeV/c, which are not used to compute the total background counts (lowest e^- energy reliable data are for 50 MeV/c beam momentum).

The beam divergence can be appreciated by looking at the relative variation of the geometrical cross section (σ_x and σ_y at full width at half maximum) for configurations a) and b) in Table II. Neglecting the data at 20 and 30 MeV/c, the divergence is a moderate ~15% at 50 MeV/c, and for momenta of 86.25 MeV/c and higher is in the range of ~1% to ~5%. We consider this deviation to be due to the inherent shape of the beam rather than diffusion through air, because the same comparison for configurations b) and c) in Table II shows that 1 mm Al affects the beam divergence by < 2 % for all momenta ≥ 50 MeV/c, and ~17 cm of air are unlikely to diffuse the beam more than 1 mm of solid aluminum.

B. Shielded detector

1) Nominal shielding characterization

The count rates relative to the e^- fraction of the particle beam are measured at the following angles: 0°, 7°, 13°, 45°, 90°, 135°, and 180°. We chose 7° because it coincides with the angle of the cone protruding from the shielding and with the MCP channels' angle. 13° is chosen because it coincides with the edge of the shielding disc (Fig. 3). For all the measurements, both the PHD and the charge per pulse distribution show the same and expected negative exponential shape (Fig. 6). The resulting count rates obtained from the exponential curve integration are summarized in Table III. The data for 20 MeV/c momentum are not listed, because the count rate after shielding was comparable to the background level, and it is not possible to assess whether this is due to an effective shielding of this radiation or to the very low beam flux. Some measurements at 30 MeV/c show a similar problem and are marked as N/A (not available).

The last column of Table III gives the integral value for an assumed isotropic environment with an e^- flux equal to the PSI beam. The weights for the numerical integration of the rates are calculated by considering the portions of sphere's surface area relative to sphere caps (0°, 180°) or segments (all other angles) whose boundaries are defined by the middle points of the cosine values between pairs of angles. Assuming an isotropic environment is an approximation, but the effect of the environment angular properties on the shielding shape will be addressed by simulations when the mission profile (orbit and attitude) and the instrument accommodation on the spacecraft will be defined in detail. The spacecraft, located to the left of Fig. 1, will act both as shielding element and as source of secondaries. It is currently under study whether its presence makes particle fluxes from a certain solid angle better or worse off to the radiation shielding.

Because the flux of primary beam's e^- varies over several decades from 20 to 345 MeV/c, we look at the ratio between detector count rate and incident beam flux, which is more indicative of the relative shielding efficacy than rates alone:

$$A_{eff}(E,\varphi) = \frac{K_{PSI}(E,\varphi)}{F_{PSI}(E)} \quad (2)$$

where K_{PSI} is the experimental count rate, and F_{PSI} is the beam flux at its focal plane (configuration a) in Table II) multiplied by the e^- fraction of the beam from Table I. The resulting quantity has the dimension of cm^{-2} MeV^{-1} and we refer to it as *"detector effective area"*. This quantity can be related to the efficacy of the radiation shielding: a higher value of A_{eff} means a larger effective cross-section of the detector, thus implying a lower capability of the shielding to reduce the radiation background (and vice versa for lower values of A_{eff}). Figure 6 shows a contour plot of A_{eff} in the investigated domain of parameters. The resulting shape is the convolution of several effects, including the variation of the spectral distribution of the radiation after the shield, the variation of the MCP intrinsic detection efficiency with angle [3], and the different thickness and geometry of shielding traversed by e^- at different angles. From this shape, we draw several conclusions.

First, A_{eff} is generally lower at 90° with respect to ± 45° departure from this direction, and 90° appears as a shallow saddle in the distribution. The decrease of A_{eff} as the angle approaches 90° can be explained by the fact that the detector cross section with respect to the beam direction varies with the cosine of the angle of incidence of the beam. From this factor only, a steep drop of A_{eff} would be expected near 90°, when the MCP are hit by particles from the side. However, the intrinsic detection efficiency of MCPs to penetrating particles increases at high incidence angles [3], thus augmenting the detector response near 90° and explaining why the saddle is not as deep as it would be expected from purely geometric considerations only. Second, the radiation shield appears most

This article has been accepted for publication in a future issue of this journal, but has not been fully edited. Content may change prior to final publication. Citation information: DOI 10.1109/TNS.2016.2614040, IEEE Transactions on Nuclear Science

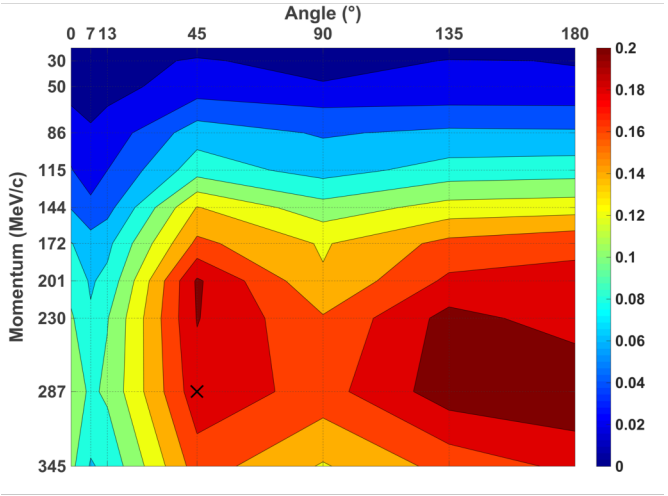

Fig. 7: Contour plot of A_{eff} (Eq. 2) in the investigated domain of beam momenta and angles. The cross (X) indicates the point at 287.5 MeV/c and 45° where experimental data are missing and the value has been extrapolated by triangulation with the neighboring points to plot a complete figure. The unit of the z direction (right color bar) is cm^2 MeV^{-1}.

effective at 0°, 7°, 13° compared to any other direction, and A_{eff} generally peaks at 45° and again at 135° – 180° at all energies. This can be explained in terms of the rather small solid angle of the MCP detector as seen from the shielding disc compared to the proximity shield. As a consequence, compared to the proximity shield, fewer scattered primary electrons and bremsstrahlung photons from the disc will reach the MCP because of a purely geometrical factor.

These observations are important to drive future optimization of shielding shape, for further reducing the background rates without increasing the shielding mass. For example, in the original simulations that led to the definition of the present shielding baseline [7] the shape of the mass model was constructed such that the material was placed as close as possible to the MCP to minimize mass. However, the experimental results show that – at parity of mass – a trade-off shall be performed between thickness and distance: a thinner shield and farther away from the MCP may actually perform better under certain geometric configurations. Moreover, the observed reduction of A_{eff} at 90° may allow reducing the shielding thickness in this direction for a minor increase in background rates, which could be more than compensated by an improved shielding effectiveness in other directions implemented by investing the saved mass at 90°. We plan to perform new simulations to optimize the shape of the NIM shielding by exploring the new solutions space now opened by these experimental insights.

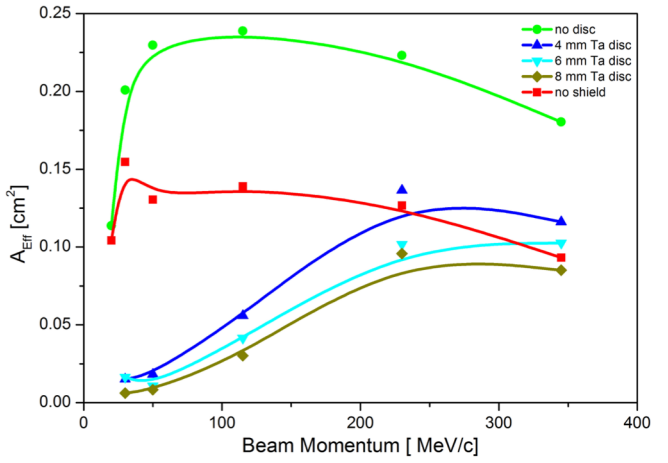

Fig. 8: MCP effective area at 0° angle with different shielding disc arrangements in front of the detector, including the measurements done with no shielding plate in green, and with a completely unshielded detector in red.

2) Shielding disc optimization

The shielding disc accounts for about 40 % of the total shielding mass, because it has to be placed at a distance of 176 mm from MCP, and therefore a significant area is needed to close the detector FoV to the external radiation environment, even if the subtended solid angle is small (0.05 sr). Fig. 8 shows the detector effective area for different shielding disc thicknesses, including the case of a completely unshielded detector (*no shield*) and of a shielded detector without the shielding disc (*no disc*).

The comparison between A_{eff} of the unshielded and of the shielded detector without disc shows that it is important to close well FoV of the opening towards the external radiation environment. A_{eff} of the former is much larger than the latter: an amplification effect implying that a significant amount of secondaries is generated in the cone protruding towards the beam direction and inside the internal cuboid cavity where the MCP is accommodated, which is directly illuminated by the beam in absence of a shielding disc.

The comparison between shielding discs of different thickness shows that a thicker disc generally provides a better shielding. On the one hand, removing 2 mm of Ta from the baseline 6 mm Ta thickness results in a significant reduction of the shield efficacy at all momenta larger than 50 MeV/c; moreover, with 4 mm of Ta for momenta larger than ~230 MeV/c the background rate on the shielded detector is higher than for the unshielded detector. On the other hand, increasing the thickness of the shielding disc to 8 mm provides a small gain in shielding effectiveness for + 30 % mass increase. In conclusion a shielding disc of 6 mm Ta remains an optimal compromise between background suppression and mass.

VI. Radiation Background Rates at Jupiter

A. Background rate in the energy range of the experiment

From the experimental count rates we calculate the expected radiation background levels in space around Europa, K_{Europa}, induced by penetrating e$^-$ in the same energy range of the investigated beam momenta by assuming an isotropic environment at Europa [1,11] and integrating the detector effective area over the whole sphere:

$$K_{Europa}(E) = A_{Eff}(E) \cdot 4\pi \cdot F_{Europa}(E) \quad (3)$$

where F_{Europa} is the differential flux of e$^-$ at Europa (# cm^{-2} s^{-1} sr^{-1}) derived from [1]. For energies where the value of F_{Europa} is not tabulated in the spectrum from [1], we derive it by linear interpolation of the natural logarithm of the differential spectra using the two closest known energy points E_0 and E_1 [8]:

$$F_{Europa}(E) = e^{\left[\ln(F(E_0))+(E-E_0)\frac{\ln(F(E_1))-\ln(F(E_0))}{E_1-E_0}\right]} \quad (4)$$

The numerical integration of Eq. 3 in the investigated e$^-$

This article has been accepted for publication in a future issue of this journal, but has not been fully edited. Content may change prior to final publication. Citation information: DOI 10.1109/TNS.2016.2614040, IEEE Transactions on Nuclear Science

energy range gives a count rate at Europa of $4.31 \cdot 10^3$ #/s.

B. Extrapolation outside the experimental energy range

Outside the investigated e^- energy range, we obtain the expected background count rates by extrapolation.

For e^- energies lower than 29.5 MeV, we perform a linear extrapolation of the count rate measured at 49.5 MeV, the lowest-energy point for which we have complete and reliable data set for all angles, by applying the following proportion:

$$\frac{K_{PSI}(49.5)}{F_{PSI}(49.5)} \cdot 1/49.5 = \frac{K_{Europa}(E)}{F_{Europa}^{4\pi}} \cdot 1/E \qquad (5)$$

Note that the first ratio in Eq. 5 is again the integral A_{eff} over the angle. This extrapolation is based on the approximation that the linear correlation of A_{eff} with the energy that can be observed between 49.5 and 172 MeV ($R^2 \geq 0.97$ at each angle) continues to hold for lower e^- energies, and on the linear scaling of radiation yield of e^- in Ta from 0 to 10 MeV [10].

For e^- energies higher than ~344.5 MeV, we assume that the detector A_{eff} is the same as we measured at 344.5 MeV/c or, in other words, that the shielding attenuates the background counts by the same amount as it does at 344.5 MeV/c (~75 % reduction compared to the differential flux, F_{Europa}).

The measured and the extrapolated rates over the complete energy range are shown in Fig. 9, together with the differential spectrum of the e^- flux at the Europa environment integrated over the MCP area. The resulting integral count rates in space are $1.37 \cdot 10^5$ #/s between 0.02 MeV and 49.5 MeV, and 23.5 #/s between 344.5 MeV and 1 GeV. The high-energy part of the spectrum appears to give a negligible contribution to the total rate to all practical effects, under the simple assumption used for this extrapolation. In contrast, the low-energy part of the spectrum is particularly critical because the radiation fluxes at Europa scales approximately with $1/E$. The total e^--induced background count rate expected in space, comprising the measured and extrapolated ranges, is $1.41 \cdot 10^5$ #/s. This rate is lower than the one obtained with an independent radiation model [12] of NIM performed as part of the complete PEP Nadir Unit ($4.10 \cdot 10^4$ #/s), thus giving a certain confidence that our extrapolations are reasonable.

Besides, previous ESA studies [11] showed that the differential e^- flux at Europa after 20 mm Al shielding flattens to a level of ~10^4 e^- cm^{-2} s^{-1} MeV^{-1}. The trend for increasing thicknesses of shielding material show that the higher the shielding thickness the higher the energy at which the spectrum becomes flat; for our shielding sandwich – equivalent to ~50 mm Al – the flattening of the spectrum after shield will likely start between 10 and 100 MeV and reach a level of ~$5 \cdot 10^3$ e^- cm^{-2} s^{-1} MeV^{-1}. Although the flux of gamma after the shield does not flatten out, but always remains about two decades lower than the input spectrum flux, by considering a typical MCP γ detection efficiency of ~2% [15] and our detector area of ~0.5 cm^2, the extrapolated rate (Fig. 9) of ~10^5 Hz/MeV appears reasonable.

C. Estimation of the mass spectra S/N

The impact of the radiation-induced noise on the mass spectrometric measurements can be estimated by superimposing the radiation background on the mass spectrum expected in space. We calculate the expected NIM mass spectrum based on the surface composition of Europa and the resulting exosphere based on various processes acting on the surfaces [9], [16], [17]. From the total e^--induced background rate in space, we derive the predicted noise level as follows:

$$N_{bin} = K_{Europa} \cdot ESF \cdot t_{bin} \cdot RR \cdot t_{meas} \cdot ADC \qquad (6)$$

where ESF is the environment safety factor, set to 2 according to ESA JUICE requirements; t_{bin} is the time width of a spectrum bin (0.5 ns); RR is the instrument repetition rate (10 kHz), t_{meas} is the measurement time (i.e., the histogram accumulation time); and, ADC is the mean digitized value of background particle counts in the spectrum expressed in dimensionless analog-to-digital units (ADU). The pulse height and charge per pulse distributions in space is the sum of a Gaussian (ion signal) and a negative exponential (penetrating particle noise). Measurements performed with a similar detector with the same MCPs used for this experiment showed that the average of the ion Gaussian PHD, the modal gain, is about 4 times higher than the exponential PHD from Co-60 γ. Given that we typically set the ADC gain so that an ion count is digitized at 5 ADU on average, we assume in Eq. 6 that the background counts contribute with 2 ADU on average.

Our experimental investigation covers only e^-, but p^+ also contribute to the total background. Because the range of p^+ in

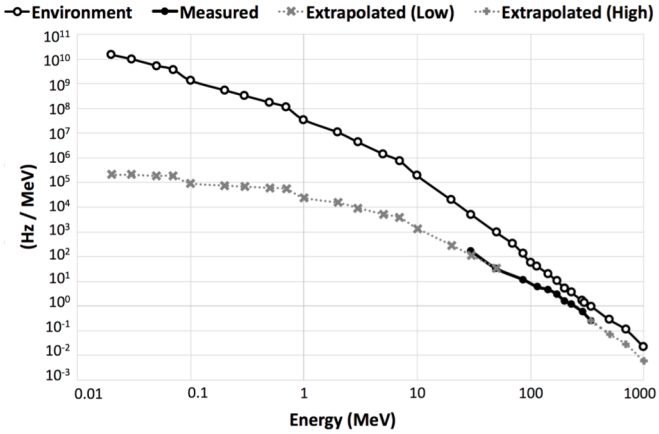

Fig. 9: Comparison between the flux of e^- at Europa through the MCP surface (environment) and the detector count rates in the measured and extrapolated ranges of e^- energies.

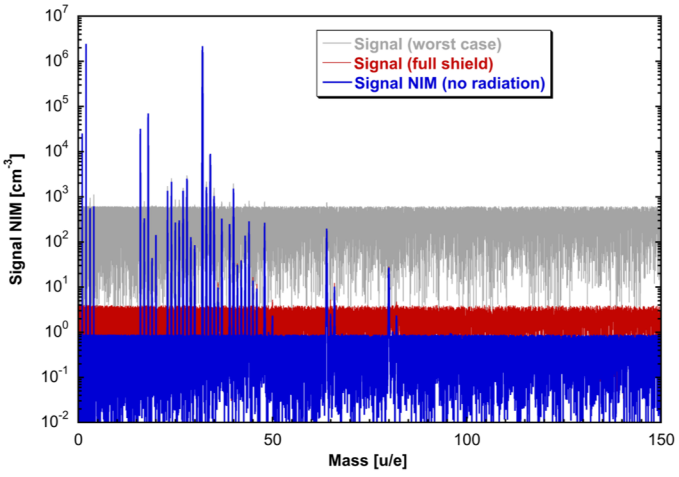

Fig. 10: Calculated NIM calibrated mass spectrum at Europa for a flyby at an altitude of 400 km, showing in red the radiation background expected after shielding. Accumulation time: 5s, repetition rate: 10 kHz.

matter is much lower than for e^- and their flux is about an order of magnitude lower than e^- [11], we add 10 % to our e^--induced background level to obtain the total background.

The resulting background height in the mass spectrum is 15 ADU, which summed to the inherent instrument electronic noise yields the predicted mass spectrum of Fig. 10. The background reduction allows to detect most of the species expected in the exosphere: the major volatiles (O, O_2, H_2, H_2O, SO_2, SO, CO_2, CO), species from non-ice surface material (Mg, MgO, Na, NaO, Ca, CaO, Al, AlO), and a few isotope ratios [17]. For completeness, we also show in Fig. 10 the background in case our low-energy extrapolation would not be valid, and a worst-case extrapolation needs to be performed. In such a scenario the radiation noise would be unacceptably high and NIM would not meet some of its science goals, because all but the most abundant species' signal would fall below the background. Moreover, the count rate would be close to MCP saturation levels [3] at ~10^7 #/s^{-1}.

VII. Conclusion

We provide an end-to-end estimation of the radiation-induced background on a TOF mass spectrometer at Jupiter's moon Europa, based on measurements with a flight-like MCP detector and shielding using an e^- beam of ~30 to ~345 MeV.

The resulting background rate in the investigated energy range, scaled for the space environment, is $4.31 \cdot 10^3$ #/s. Extrapolating the experimental data to cover the entire energy spectrum at Europa, we obtain a total background rate of $1.41 \cdot 10^5$ #/s. Because the total background in space depends heavily on the contribution by e^- of energy < ~10 MeV, we plan to verify the validity of the low-energy extrapolation with new experimental measurements with a few MeV e^-. Additionally, we aim at performing measurements ~500 MeV e^-, to get insight into the effect of particle showers on the detector. Finally, we are analyzing of the results of a detailed Geant4 model of this measurement campaign, which will provide more insights into the experimental observations and the opportunity to use the correlated model to simulate the detector response to the full space radiation environment.

These results demonstrate how to shield an MCP detector for a TOF mass spectrometer at Jupiter, including details of the shielding design and of the methods followed to derive the expected count rates in space. Moreover, we provide directions for the optimization of shielding geometry, and a set of measurements that can be used by modelers to correlate their radiation simulations with experimental data.

Given that Jupiter and its moons will be the target of several confirmed and proposed missions in the next decades, such as ESA's JUICE, NASA's Europa Multiple Flyby Mission and Europa lander, these results are of general relevance to design radiation shielding for MCPs and other flux-critical detectors (e.g., channel electron multipliers) on instruments bound to measure in the harsh Jovian radiation environment.

Acknowledgment

We thank S. Brüngger and H. Mischler for designing and manufacturing the test setup, and A. Vorburger, M. Neuland, A. Péteut, T. Uthaicharoenpong, and R. Wiesendanger for their help during the measurements at the PSI facilities.

References

[1] "JUICE environment specification", ESA, Noordwijk, The Netherlands, Rep. JS-14-09 v5.4, Jun. 20, 2015.

[2] M. Tulej, S. Meyer, M. Lüthi, D. Lasi, A. Galli, L. Desorgher, W. Hajdas, S. Karlsson, L. Kalla, and P. Wurz, "Detection efficiency of microchannel plates for e(-) and π(-) in the momentum range from 17.5 to 345 MeV/c," *Rev. Sci. Instrum.*, vol. 86, pp. 083310-1–083310-12, Aug. 2015.

[3] M. Tulej, S. Meyer, M. Lüthi, D. Lasi, A. Galli, D. Piazza, L. Desorgher, D. Reggiani, W. Hajdas, S. Karlsson, L. Kalla and P. Wurz, "Experimental investigation of the radiation shielding efficiency of a MCP detector in the radiation environment near Jupiter's moon Europa," *Nucl. Instr. Meth. B*, vol. 383, pp. 21–37, Sep. 2016.

[4] W. Hajdas, L. Desorgher, K. Deiters, D. Reggiani, T. Rauber, M. Tulej, P. Wurz, M. Lüthi, L. M., K. Wojczuk, and P. Kalaczynski, "High energy electron radiation exposure facility at PSI," *J. Appl. Math. and Phys.,* vol. 2, pp. 910–917, Aug. 2014.

[5] W. C. Fan, C. R. Drumm, S. B. Roeske, and G. J. Scrivner, "Shielding considerations for satellite microelectronics," *IEEE Trans. Nucl. Sci.*, vol. 43, no. 6, pp. 2790–2796, Dec. 1996.

[6] L. Desorgher, "Radiation simulation study for the PEP-NU on the LAPLACE mission," SpaceIT GmbH, Bern, Switzerland, Rep. JGO-PEP-TN-0901 v1.0, Mar. 23, 2010.

[7] T. Knight and M. Grande, "NIM Radiation shielding design development," University of Aberystwyth, May 26, 2015.

[8] G. Santin, "JUICE spectra interpolation," ESA, Noordwijk, The Netherlands, Tech. Memo. TEC-EES/2015.92/GS, Oct. 1, 2015.

[9] M. Pfleger, J. Lindkvist, H. Lammer, M. Holmström, A. Vorburger, H. I. M. Lichtenegger, P. Wurz, and S. Barabash, "3D-modeling of Callisto's surface sputtered exosphere environment," submitted for publication.

[10] M. J. Berger, J. S. Coursey, M. A. Zucker, and J. Chang, "ESTAR, PSTAR, and ASTAR: Computer Programs for Calculating Stopping-Power and Range Tables for Electrons, Protons, and Helium Ions," version 1.2.3, National Institute of Standards and Technology, Gaithersburg, MD, 2005. [Online] Available: http://physics.nist.gov/PhysRefData/Star/Text/ESTAR.html. Accessed on: Aug. 20, 2016.

[11] "JUICE environment specification," ESA, Noordwijk, The Netherlands, Rep. JS-14-09 v5.1, Oct. 15, 2013.

[12] S. Karlsson, "PEP radiation modelling report (PA-06.01)," Rep. JUI-IRF-PEP-RP-002 v1.0, Jun. 1, 2016.

[13] G. Santin, V. Ivanchenko, H. Evans, P. Nieminen, and E. Daly, "GRAS: a general purpose 3-D modular simulation tool for space environment effects analysis," *IEEE Trans. Nucl. Sci.*, vol. 52, pp. 2294–2299, Dec. 2005.

[14] J. Allison, K. Amako, J. Apostolakis, H. Araujo, P. Arce Dubois, M. Asai, G. Barrand, R. Capra, S. Chauvie, R. Chytracek, G. A. P. Cirrone, G. Cooperman, G. Cosmo, G. Cuttone, G. G. Daquino, M. Donszelmann, M. Dressel, G. Folger, F. Foppiano, J. Generowicz, V. Grichine, S. Guatelli, P. Gumplinger, A. Heikkinen, I. Hrivnacova, A. Howard, S. Incerti, V. Ivanchenko, T. Johnson, F. Jones, T. Koi, R. Kokoulin, M. Kossov, H. Kurashige, V. Lara, S. Larsson, F. Lei, O. Link, F. Longo, M. Maire, A. Mantero, B. Mascialino, I. McLaren, P. Mendez Lorenzo, K. Minamimoto, K. Murakami, P. Nieminen, L. Pandola, S. Parlati, L. Peralta, J. Perl, A. Pfeiffer, M. G. Pia, A. Ribon, P. Rodrigues, G. Russo, S. Sadilov, G. Santin, T. Sasaki, D. Smith, N. Starkov, S. Tanaka, E. Tcherniaev, B. Tomé, A. Trindade, P. Truscott, L. Urban, M. Verderi, A. Walkden, J. P. Wellisch, D. C. Williams, D. Wright, and H. Yoshida, "Geant4 developments and applications," *IEEE Trans. Nucl. Sci.*, vol. 53, pp. 270–278, Feb. 2006.

[15] Y. T. Tanaka, I. Yoshikawa, K. Yoshioka, T. Terasawa, Y. Saito, and T. Mukai, "Gamma-ray detection efficiency of the microchannel plate installed as an ion detector in the low energy particle instrument onboard the GEOTAIL satellite," *Rev. Sci. Instr.*, vol. 78, pp. 034501-1–034501-4, Mar. 2007.

[16] A. Vorburger, P. Wurz, H. Lammer, S. Barabash, and O. Mousis, "Monte-Carlo simulation of Callisto's exosphere," *Icarus,* vol. 262, pp. 14–29, Dec. 2015.

[17] P. Wurz, A. Vorburger, A. Galli, M. Tulej, N. Thomas, Y. Alibert, S. Barabash, M. Wieser, and H. Lammer, "Measurement of the atmospheres of Europa, Ganymede, and Callisto," European Planetary Science Congress, in *EPSC Abstracts*, 2014, vol. 9, id. EPSC2014-504.